

Article

# Scanning Inside Volcanoes with Synthetic Aperture Radar Echography Tomographic Doppler Imaging

Filippo Biondi <sup>†</sup>

Department of Electronic and Electrical Engineering, University of Strathclyde, Glasgow G1 1XW, UK; filippo.biondi@marina.difesa.it; Tel.: +39-335-833-4216

<sup>†</sup> Current address: Via Luca Benincasa 21/B Corciano, 06073 Perugia, Italy.

**Abstract:** A problem with synthetic aperture radars (SARs) is that due to the poor penetrating action of electromagnetic waves within solid bodies, the ability to see through distributed targets is precluded. In this context, indeed, imaging is only possible for targets distributed on the scene surface. This work describes an imaging method based on the analysis of micro-motions present in volcanoes and generated by the Earth's underground heat. Processing the coherent vibrational information embedded in a single SAR image, in the single-look-complex configuration, the sound information is exploited, penetrating tomographic imaging over a depth of about 3 km from the Earth's surface. Measurement results are calculated by processing a single-look-complex image from the COSMO-SkyMed Second Generation satellite constellation of Vesuvius. Tomographic maps reveal the presence of the magma chamber, together with the main and the secondary volcanic conduits. This technique certainly paves the way for completely new exploitation of SAR images to scan inside the Earth's surface.

**Keywords:** synthetic aperture radar; Doppler frequencies; multi-chromatic analysis; micro-motion; volcanoes; seismic images



**Citation:** Biondi, F. Scanning Inside Volcanoes with Synthetic Aperture Radar Echography Tomographic Doppler Imaging. *Remote Sens.* **2022**, *14*, 3828. <https://doi.org/10.3390/rs14153828>

Academic Editor: Sonia Calvari

Received: 24 April 2022

Accepted: 25 July 2022

Published: 8 August 2022

**Publisher's Note:** MDPI stays neutral with regard to jurisdictional claims in published maps and institutional affiliations.



**Copyright:** © 2022 by the author. Licensee MDPI, Basel, Switzerland. This article is an open access article distributed under the terms and conditions of the Creative Commons Attribution (CC BY) license (<https://creativecommons.org/licenses/by/4.0/>).

## 1. Introduction

Vesuvius is an active volcano and dominates the central part of the Campanian coast, located in Italy. The morphology of the volcanic complex (including the Campi Flegrei) clearly reveals its active nature, characterized by eruptive cones and magmatic fluids flows [1]. From a morphological point of view, Vesuvius is a volcanic complex composed of Mount Somma, whose activity ended with the formation of a summit caldera. All this has led to Vesuvius being characterized as one of the most dangerous volcanoes in the world [2]. The reinterpretation of the volcanological and historical evidence shows that the eruption of Vesuvius in 79 AD consisted of two main phases. The initial Plinian phase, lasting 18–20 h, caused a large pumice fallout, resulting in the slow accumulation of a layer of pumice up to 2.8 m thick over Pompeii and other regions to the south [3]. Research [4] gave the general model for the behaviour of the Somma-Vesuvius, distinguishing three classes in the eruptive pattern. The authors of [5] gave the seismic evidence of an extended magmatic sill under Vesuvius. The authors found evidence of an extended (at least 400 km<sup>2</sup>) low-velocity layer at about 8 km depth. The inferred seismic velocities (about 2.0 km/s), as well as other evidence, indicate an extended sill with magma interspersed in a solid matrix.

The velocity structure of the Somma-Vesuvius volcano, obtained by joint inversion of P-and S-wave arrival times from both local earthquakes and shot data collected during the TOMOVES 1994 and 1996 experiments, is presented in [6]. The entire seismic catalog available from 1987 to 2000 (1003 events) was relocated in the 3D velocity model obtained. The thermal model and the 2D numerical scheme of the Vesuvius magma chamber, locating it at a depth of approximately 6 km, has been studied in [7]. Given the high risk of the Vesuvius crater, an efficient numerical modeling and the methodology adopted to evaluate the resistance of buildings under the combined action of volcanic phenomena is developed in [8].

Numerous works have been carried out in the field of sonic-inspired imaging, especially in the medical field, through the use of ultrasound. Theoretical studies conducted in the early 1980s suggested that ultrasonic imaging using the correlation technique can overcome some of the drawbacks of classical pulse echography. An efficient high-resolution technique was developed in [9] by transmitting coded signals using high-frequency transducers, up to 35–50 MHz, for ophthalmic echography to image fine eye structures. The first high-frequency echographic images obtained with the prototype probe are presented in [10]. An attractive description of the first mechanical scanning probe for ophthalmic echography based on a small piezoelectric ultrasound motor is reported in [11]. A novel method for line restoration in speckle images addressing a sparse estimation problem using both convex and non-convex optimization techniques is reported in [12]. Lung ultrasound imaging is a fast evolving field of application for ultrasound technologies. The authors of [13] design an image formation process to work on lung tissue, and ultrasound images are generated with four orthogonal bands centered at 3, 4, 5, and 6 MHz which can be acquired and displayed in real time.

In the field of seismic tomography, several works have been carried out. In [14], scientific methods are developed for the design of linear tomographic reconstruction algorithms with specified properties. An experimentation reconstruction method for seismic transmission travel-time tomography was developed in [15]. The method is implemented via the combinations of singular value decomposition, appropriate weighting matrices, and variable regularization parameters. A cross-correlation of environmental seismic noise from 1 month of recordings at USArray stations in California that produced hundreds of seismic wave group velocity measurements was implemented in [16]. The authors used data to construct tomographic images of the principal geological units of California, with low-speed anomalies corresponding to the main sedimentary basins and high-speed anomalies corresponding to the igneous cores of the major mountain ranges. In [17], ambient seismic noise signal processing demonstrated the feasibility of measuring very small relative seismic velocity perturbations in the order of 0.05%. The ability to record volcanic edifice inflation in this way should improve the ability to predict eruptions, their intensity, and the potential environmental impact.

The foundations of diffraction tomography for offset vertical seismic profiling and well-to-well tomography are presented in [18]. Computer simulations are used for underground vertical seismic profiling. The influence of quality in tomographic reconstructions obtained via the filtered back-propagation algorithm is investigated in [19]. To better understand the volcanic phenomena acting on Montserrat, a subset of the data, recorded at several land stations located from the southeast to the northwest line, was analyzed in [20]. The resulting velocity model reveals the presence of high-velocity underground body movements at the volcanic edifice cores. The development and assessment of three novel muon tracing methods and two scattering angle projection methods for muon-tomography are provided in [21]. The reconstructed images shows an expected improvement in image quality when compared with conventional techniques. Three-dimensional models of the P-wave velocity ( $V_p$ ), the ratio of P- to S-wave velocity ( $V_s$ ),  $(\frac{V_p}{V_s})$ , and the P-wave quality factor ( $Q_p$ ) are determined [22].  $V_p$  and  $(\frac{V_p}{V_s})$  models were determined by jointly inverting P travel times and S-P travel-time intervals, and a  $Q_p$  model by inverting  $t * \frac{t}{Q_p}$  observations derived from modeling the velocity amplitude spectrum of P wave arrivals. The upper crustal isotropic and radial anisotropic structures of the Jeju Island offshore Volcano were imaged in [23]. Results of an ambient seismic noise tomography study of the Merapi–Merbabu complex are presented in [24]. A seismic survey for the characterization of the main subsurface features of the Solfatara was developed in [25]. Using the complete dataset, the authors carried out surface wave inversion with high spatial resolution. A classical minimization of a least-squares objective function was computed to retrieve the dispersion curves of the surface waves. The recognition and localization of magmatic fluids are prerequisites for evaluating the volcano hazard of the highly urbanized area of Mt Vesuvius. Evidence and constraints for the volumetric estimation of magmatic fluids underneath this

sleeping volcano were studied in [26]. Experimental measurements revealed the presence of magma at relatively shallow depths. The volume of fluids (approx.  $30 \text{ km}^3$ ) is sufficient to contribute to future explosive eruptions. Finally, controlled source audio-magnetotelluric sounding tomography performed in the past in the volcanic area of Mt. Vesuvius by [27] allowed a reliable electrical structure to be recovered down to a few km of depth.

In the field of vibration estimation by processing SAR images, there are other relevant works. A new critical infrastructure monitoring procedure was developed in [28]. The technique was applied by processing COSMO-SkyMed data to detect and monitor the destabilization of the Mosul dam, which is the largest hydraulic structure in Iraq. The procedure consists of an in-depth modal evaluation based on micro-motion (m-m) estimation through Doppler tracing of sub-apertures and multi-chromatic analysis (MCA). On the other hand, a comprehensive damage detection procedure was designed using micro-motion estimation of critical sites based on modal property analysis developed in [29]. Specifically, the m-m is processed to extract modal features such as natural frequencies and mode shapes generated by large infrastructure vibrations. Several case studies were considered, and the "Morandi" bridge (Polcevera Viaduct) in Genoa, Italy, was analyzed in depth, highlighting anomalous vibration modes in the period before the bridge collapse. After conducting a deep analysis of the state of the art, it becomes clear that to date there is a lack of a versatile, cost-effective, and widely applicable tool for internal monitoring of volcanoes. In this context, a new method that employs m-m estimation to perform deep scanning of volcanoes is presented. This approach appears to be tailored to fill this gap technology when today there is direct access to SAR satellite data, which is a day–night sensor, and is also able to penetrate clouds.

The experimental results are obtained by processing one SAR Spotlight image, observing Vesuvius, and revealing its internal structure. Tomographic maps show the main crater section, the volcanic conduit, and the main vent. In depth, the magma chamber and the presence of a secondary magmatic fluid conduit are also visible. In addition, the internal structure of the currently plugged main magmatic fluid conduit reveals several different structures of debris layers.

## 2. Methodology

In this work, the m-m technique is used to perform sonic imaging by processing a single synthetic aperture radar (SAR) image in the single-look-complex (SLC) configuration. The technique involves the m-m estimation belonging to the Vesuvius volcano and is generated by the intensive underground seismic activity that reflects superficial vibrations. The m-m estimation is carried out through MCA, performed in the Doppler direction. Multiple Doppler sub-apertures, SAR images with lower azimuth resolution, are generated to estimate the vibrational trend of some pixels of interest. The infra-chromatic displacement is calculated through the pixel-tracking technique [30,31], using high-performance sub-pixel coregistration [28,29]. Vibrations observed along the tomographic view direction, embedded into the multi-chromatic Doppler diversity, are focused along the height (or depth) dimension, and develop high-resolution tomographic underground imaging.

The SAR synthesizes the electromagnetic image through a "side looking" acquisition, according to the observation geometry shown in Figure 1, where:

- $r$  is the zero-Doppler distance (constant);
- $R$  is the slant-range;
- $R_0$  is the reference range at  $t = 0$ ;
- $d_a$  is the physical antenna aperture length;
- $V$  is the platform velocity;
- $d$  is the distance between two range acquisitions;
- $G_{sa}$  is the total synthetic aperture length;
- $t$  is the acquisition time variable;
- $T$  is the observation duration;
- $t = 0$  and  $t = T$  are the start and stop time acquisition, respectively;

- $L = \frac{\lambda r}{d_a}$  is the azimuth electromagnetic footprint width;
- $\theta$  is the incidence angle of the electromagnetic radiation pattern.

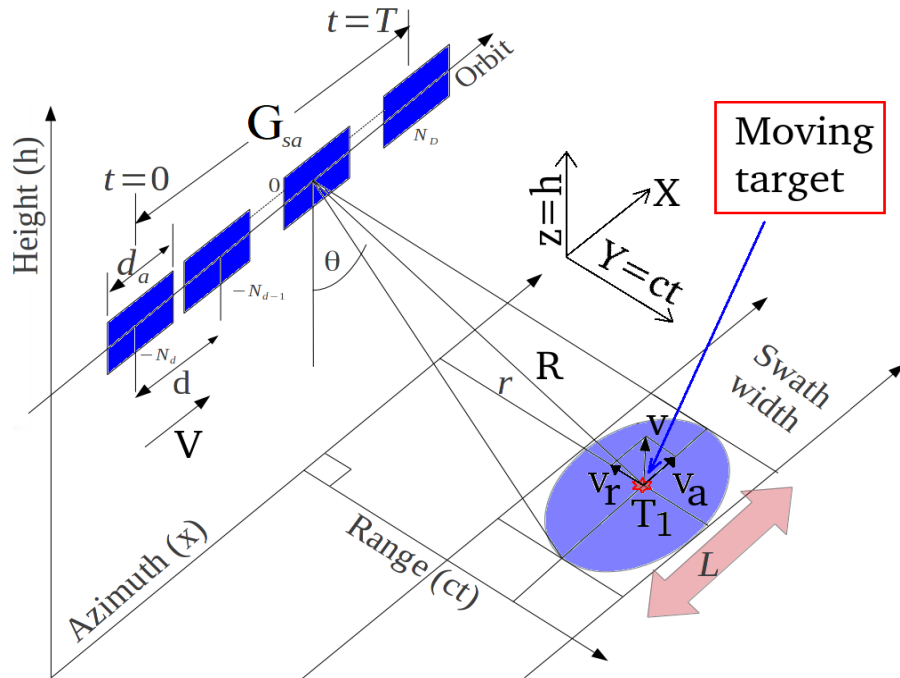


**Figure 1.** SAR acquisition geometry.

All the above parameters are related to the staring-spotlight SAR acquisition that is adopted in this work. Considering what is formalized in Appendix A, the MCA technique, based on Doppler sub-apertures, is used to estimate the following master–slave pixel shift complex parameters (A12):

- $\epsilon_{r_1} = \frac{v_r}{V}$  (due to range velocity);
- $\epsilon_{r_2} = \frac{a_r R_0}{V^2}$  (due to range acceleration);
- $\epsilon_{c_1} = \frac{v_c}{V}$  (due to azimuth velocity).

Thus, the above terms modify the received signal, as shown in [32], and should be taken into account in Equation (A6).

## 2.1. Tomographic Model

Considering a single SLC image from which we applied the MCA according to the frequency allocation strategy depicted in Figure 2, the tomogram represented by the line of contiguous pixels shown in Figure 3 is calculated. The vibrations present on the tomographic plane extending from the Earth's surface to a depth of a few kilometres is assessed. The figure represents a series of harmonic oscillators anchored on each pixel of the tomographic line, symbolically represented as a spring linked to a mass and oscillating due to the application of harmonic vibrations. Each wave generated by each harmonic oscillator bounces off the surface of the Earth as there is an abrupt variation in the density of the medium (the ground–air boundary). On each pixel, a vibrational phasor is observed in time applying Doppler MCA [28,29]. Through the orbital change of view (which is performed in azimuth), an effective subsurface in-depth vibrational scan of the Earth is achieved.

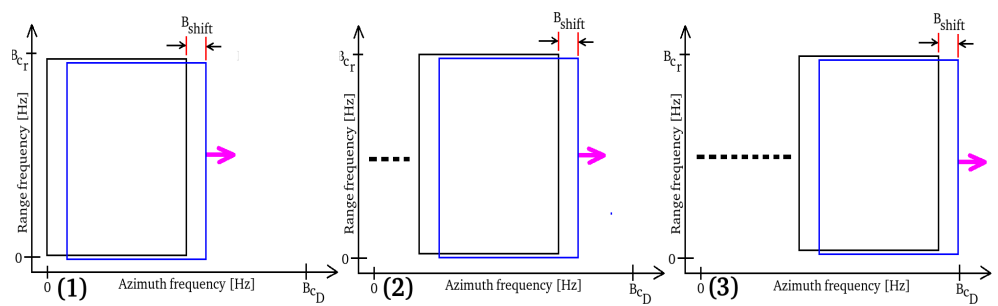


**Figure 2.** Doppler sub-aperture strategy. (1) Spectrum explored from the beginning. (2) Spectrum explored from the middle. (3) Finally explored spectrum.

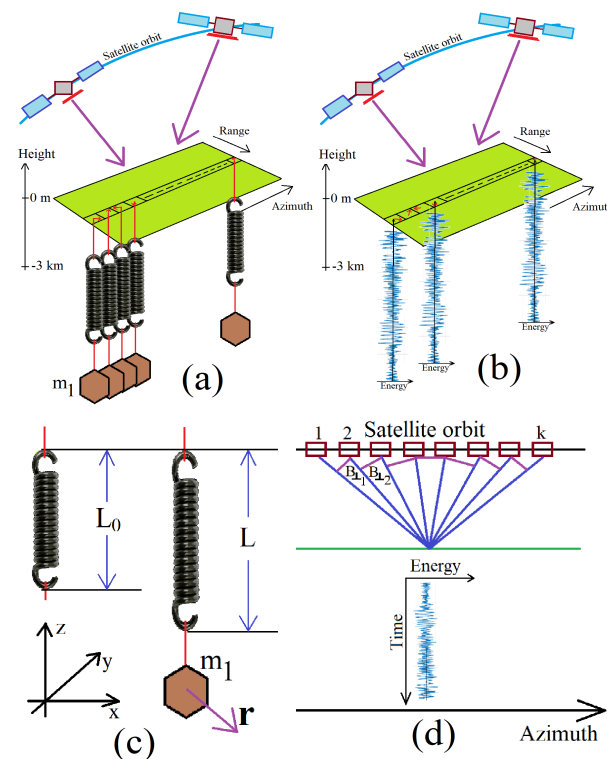


**Figure 3.** Tomographic acquisition geometry. (a) Orbital geometry with the schematic representation of moving masses on the considered pixels. (b) Orbital geometry with the measured vibrations present on the considered pixels. (c) Details of the spring-mass scheme. (d) orthogonal baseline scheme for tomography.

## 2.2. Vibrational Model of the Earth

The proposed vibrational model of the Earth's surface is schematically shown in Figure 3a,b. The geometrical reference system for both sub-pictures is the range, azimuth and altitude three-dimensional space. For the present case, the vertical dimension represents the depth below the topographic level (for this specific case the medium boundary is represented by the green plane). The tomographic line of interest is constituted of the series of contiguous pixels laying on the green plane. As can be seen from Figure 3a, on each pixel belonging to the tomographic line, a mass is hanging using a spring. This system is now induced to oscillate harmonically, helped by the Earth magma instability. These oscillations are schematized as the vibration energy function visible in Figure 3b. In this context, the radar instantaneously perceives this coherent harmonic oscillation. From a mathematical point of view, the Earth's displacement is perceived as a complex shift belonging on each pixel of interest. Each instantaneous displacement is estimated between the master image with respect to the slave, where oversimplification shifts are estimated through the pixel

tracking technique [28,29]. The number of tomographic independent looks (depending on the total number of Doppler sub-apertures) is defined by the parameter  $k$ .

We suppose now the spring being perturbed by an impulsive force. According to this perturbation, the rope begins to vibrate, describing a harmonic motion (in this context we are not considering any form of friction). The resulting perturbation moves the rope through the space-time in the form of a sinusoidal function. The seismic wave will then reach a constraint end that will cause it to reflect in the opposite direction. The reflected wave will then reach the opposite constraint that will make it reflect in the original direction and return to the initial location, maintaining the same frequency and amplitude. According to classical physics principles, the rebounding wave is superimposed on the arriving wave, and the interference of two sine waves with the same amplitude and frequency propagating in opposite directions leads to the generation of an ideal and perpetual standing wave on the spring. Each vibrational channel is now considered when the spring is able to oscillate into the three-dimensional space, according to specific perturbation nature. When the Earth vibrates, it happens that the length of the spring must also fluctuate. This phenomenon causes oscillations in the tension domain of the spring. It is clear that these oscillations (i.e. the longitudinal ones) propagate through a frequency approximately twice as high as the frequency value of the transverse vibrations. The coupling between the transverse and longitudinal oscillations of the spring can essentially be modeled through non-linear phenomena.

Figure 3c,d illustrates the oscillating model in the Euclidean space–time coordinates  $(x,y,z,t)$ , where the satellite motion has been purified from any orbital distortions, so that the geometric parameters used to perform the tomographic focusing can be rigorously understood. From Figure 3c,  $L$  is the length of the spring when it is at its maximum tension while  $L_0$  is its length when no mass is present. Finally, the spring has been considered to have an elastic constant equal to  $\xi$ . The vibrational force applied to the mass  $m_1$  of Figure 3c is equal to [33]:

$$F = -4\xi \mathbf{r} \left( 1 - \frac{L_0}{\sqrt{L^2 + 4\mathbf{r}^2}} \right). \quad (1)$$

if  $\mathbf{r} \ll L$ , (1) is expanded in the following series:

$$F = -4\xi \mathbf{r} (L - L_0) \left( \frac{\mathbf{r}}{L} \right) - 8\xi L_0 \left[ \left( \frac{\mathbf{r}}{L} \right)^3 - \left( \frac{\mathbf{r}}{L} \right)^5 + \dots \right], \quad (2)$$

where a precise approximation of (2) is the following cubic restoring force:

$$F = m\ddot{\mathbf{r}} \approx -4\xi \mathbf{r} (L - L_0) \left( \frac{\mathbf{r}}{L} \right) \left[ 1 + \frac{2L_0}{(L - L_0)} \left( \frac{\mathbf{r}}{L} \right)^2 \right]. \quad (3)$$

Considering (3), the non-linearity dominates when  $L \approx L_0$ . If we define:

$$\omega_0 = \frac{4\xi}{m} \left[ \frac{(L - L_0)}{L} \right], \quad (4)$$

and

$$\xi = \frac{2L_0}{L^2} (L - L_0). \quad (5)$$

Considering (3), we have:

$$\ddot{\mathbf{r}} + \omega^2 \mathbf{r} \left( 1 + \xi \mathbf{r}^2 \right) = 0. \quad (6)$$

if we consider damping and forcing (6) is modified as:

$$\ddot{\mathbf{r}} + \lambda \dot{\mathbf{r}} + \omega^2 (1 + \xi \mathbf{r}^2) \mathbf{r} = \mathbf{f}(\omega t), \quad (7)$$

where  $\mathbf{f}(\omega t)$  is the forcing term and  $\lambda$  is the damping coefficient. If non-linearity of (7) is sufficiently low, it can be reduced to the following two-degrees-of-freedom linear harmonic oscillator:

$$\mathbf{r}(t) = (a \cos \omega_0 t, b \sin \omega_0 t) \exp\left(\frac{-\lambda t}{2}\right). \quad (8)$$

In (8),  $\{a, b\}$  are the instantaneous shifts estimated by the coregistrator. The harmonic oscillator (8) is the displacement parameters  $\epsilon_{r_1}, \epsilon_{r_2}, \epsilon_{c_1}$  estimated by (A12). According to Figure 3d, the vector representation of  $k$  samples of the time-domain function (8) consisting in the following multi-frequency data input is considered:

$$\mathbf{Y} = [\mathbf{y}(1), \dots, \mathbf{y}(k)], \in \mathbf{C}^{k \times 1}. \quad (9)$$

The steering matrix  $\mathbf{A}(z) = [\mathbf{a}(z_{min}), \dots, \mathbf{a}(z_{MAX})], \in \mathbf{C}^{k \times F}$  contains the phase information of the Doppler frequency variation of the sub-aperture strategy, associated with a source located at the elevation position  $\mathbf{z} \in \{z_{min}, z_{MAX}\}$ ,

$$\mathbf{A}(\mathbf{K}_z, \mathbf{z}) = \begin{bmatrix} 1, \exp(j2\pi k_{z_2} t z_0), \dots, \exp(j2\pi k_{z_{k-1}} t z_0) \\ 1, \exp(j2\pi k_{z_2} t z_1), \dots, \exp(j2\pi k_{z_{k-1}} t z_1) \\ \dots \\ 1, \exp(j2\pi k_{z_2} t z_{F-1}), \dots, \exp(j2\pi k_{z_{k-1}} t z_{F-1}) \end{bmatrix}, \quad (10)$$

where  $\mathbf{K}_z = \frac{4\pi B_\perp}{\lambda \mathbf{r}_i \sin \theta}, i = 1, \dots, k$ ,  $B_\perp$  is the  $i$ -th orthogonal baseline, which is visible in Figure 3d, and  $\mathbf{r}_i$  is the  $i$ -th slant-range distance. The standard sonic tomographic model is given by the following relation:

$$\mathbf{Y} = \mathbf{A}(\mathbf{K}_z, \mathbf{z}) \mathbf{h}(\mathbf{z}). \quad (11)$$

where in (11)  $\mathbf{h}(\mathbf{z}) \in \mathbf{C}^{1 \times F}$ , inverting (11) I finally find the following tomographic solution:

$$\mathbf{h}(\mathbf{z}) = \mathbf{A}(\mathbf{K}_z, \mathbf{z})^\dagger \mathbf{Y}. \quad (12)$$

In (12), the steering matrix  $\mathbf{A}(\mathbf{K}_z, \mathbf{z})$  represents the best approximation of a matrix operator performing the digital Fourier transform (DFT) of  $\mathbf{Y}$ . The tomographic image  $\mathbf{h}(\mathbf{z})$ , which represents the spectrum of  $\mathbf{A}(\mathbf{K}_z, \mathbf{z})$ , is obtained by carrying out pulse compression.

The tomographic resolution is equal to  $\delta_T = \frac{\lambda R}{2A}$ , where  $\lambda$  is the sound wavelength over the earth,  $R$  is the slant range, and  $A$  is the orbit aperture considered in the tomographic synthesis; in other words, it consists in the Doppler bandwidth used to synthesize the sub-apertures. The maximum tomographic resolution obtainable using this SLC data, synthesized at 24 kHz, is as follows. Considering an average speed of propagation of the seismic waves of about  $v \approx 3500 \frac{\text{km}}{\text{h}}$  (approximately  $972 \frac{\text{m}}{\text{s}}$ ), a frequency of investigation set by us equal to 200 Hz, the wavelength of these vibrations is equal to about  $\lambda = \frac{v}{f} \approx \frac{3500}{200} \approx 4.86 \text{ m}$ . Considering the above parameters, extending the tomography to the maximum orbital aperture equal to half the total length of the orbit, therefore about 42,000 m, with  $R = 650,000 \text{ m}$ , the tomographic resolution is equal to  $\delta_z = \frac{\lambda R}{2A} = \frac{4.86 \cdot 650,000}{2 \cdot 42,000} \approx 36 \text{ m}$ . This is the tomographic resolution set to calculate all the experimental parts shown in Section 3.

### 2.3. Computational Scheme

Here, the computational steps required to perform seismic tomography are explained. This subsection is proposed to effectively explain the computational scheme to ensure the repeatability of the experiments. The computational scheme, consisting of 11 interconnected

blocks, is depicted in Figure 4. Block number 1 contains the SAR image in SLC format, processed to obtain tomography, while block number 2 represents the two-dimensional DFT (DFT2) operator. The input of computational stages 3 and 4 represents the copy of the DFT2 of 1, and therefore contains the same data, having a common source. Computational stage 3 is programmed to generate the sub-aperture represented by the black squared Doppler spectrum visible in Figure 2, while block 4 is programmed to generate the blue squared spectrum, also visible in Figure 2. Computational blocks 5 and 6 perform the inverse DFT2 (IDFT2) which is used to return to a lower azimuth resolution SLC SAR image. Computational block 7 performs pixel-tracking for all those pixels for which tomography needs to be trained. The result of pixel-tracking is the generation of complex vectors that will form block 8 (non-computational), which represents the raw tomographic complex data that must be focused on in elevation or depth but in the orthogonal dimension of the slant range. The focus of the raw tomographic signal is effected by computational block 9, representing the DFT mathematical operator. Block 10 (this is also not computational) represents the focused tomographic image. Finally, block 11 performs the geocoding of the tomogram, using a three-dimensional geographic coordinate reference system.

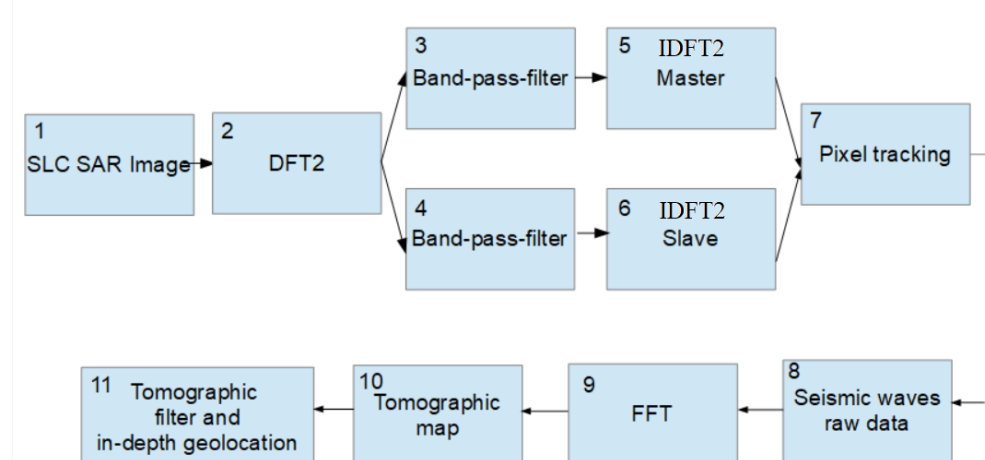


**Figure 4.** Computational scheme of tomographic imaging.

### 3. Experimental Results

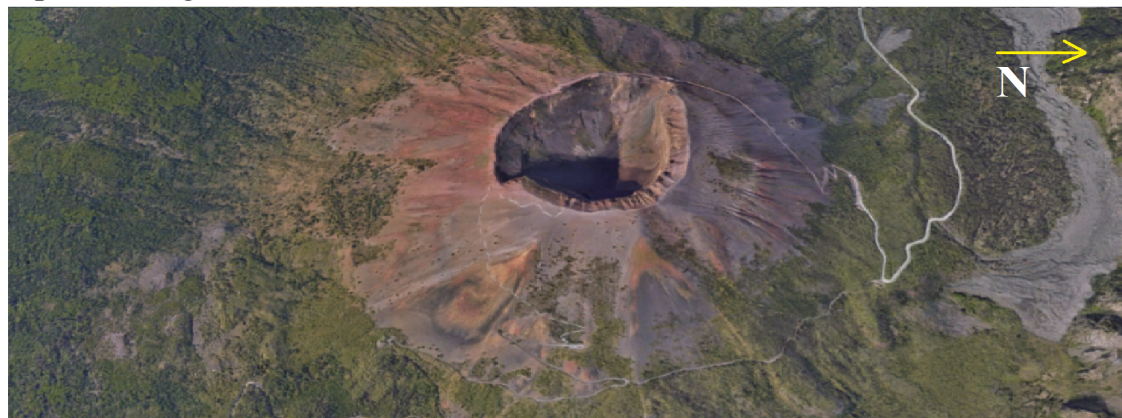
In this section, all the experimental results are described by processing a SAR image acquired by the COSMO-SkyMed Second Generation (CSG) satellite constellation. The data concerns a spotlight-2A acquisition mode, in the horizontal–horizontal (HH) polarization, with a Doppler band of about 22.5 kHz, and a chirp band of about 450 MHz. For this first case study, both the optical and the SLC image in magnitude are depicted in Figure 5a,b, respectively. The characteristics of the employed SAR image are listed in Table 1. Figure 6a is the representation of the SAR (magnitude) image where Vesuvius with its main crater is visible. Yellow line 1 is where the seismic tomogram is calculated. The test dataset is constituted by an entire range line belonging between the near range and the far range of the SAR image. Figure 6b is the result representing the estimated seismic tomography. The depth of investigation is about 3 km. In the figure, the surface topography of the volcano and its entire interior are visible. From the tomogram, it is possible to observe the crater of the main conduit inside red box 1. From this result, we observe the presence of vibration energy accumulations located in depth. This discontinuity suggests the presence of material that vibrates more concerning the background. This anomaly could be associated with the presence of denser material, and therefore with a sort of cap located below the main crater of Vesuvius. On the left side of the cap, there are two ducts, probably created by the pressure of the vapors or fluid gasses coming from underground. The maximum depth measured by the tomogram is approximately 3 km from the maximum topographic surface height of the volcano. Figure 6a,b is a detailed analysis of the of the volcano feeder conduit. In this figure, two apertures, probably excavated by high-pressure magmatic fluid gases,

and the presence of a large portion of a denser material (having higher vibrational energy), residing below the surface of the main crater at a depth of about 1 km, are visible.

**Table 1.** Characteristics of the SAR acquisitions.

SAR Parameter	Value
Chirp bandwidth	450 MHz
Doppler Bandwidth	22 kHz
PRF	2·(Doppler bandwidth)
Antenna length	6 m
Type of acquisition	Spotlight
Polarization	HH
Acquisition duration	14 s
Platform velocity	7 km/s
Observation height	650,000 m
Acquisition date	17 January 2022 m
Acquisition geometry	Right-ascending

Optical image



SLC image (magnitude)

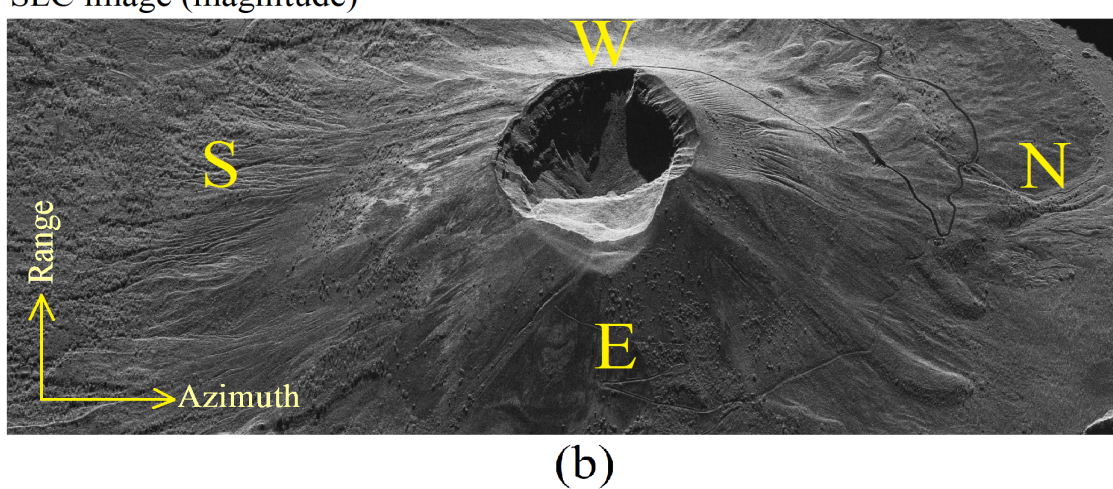


**Figure 5.** Environment images. (a) optical image. (b) SLC SAR image in magnitude.

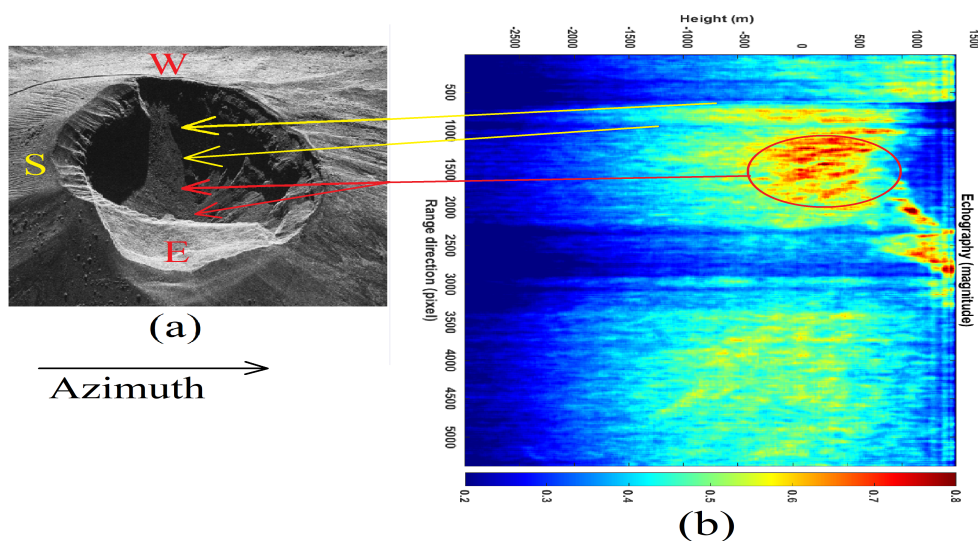
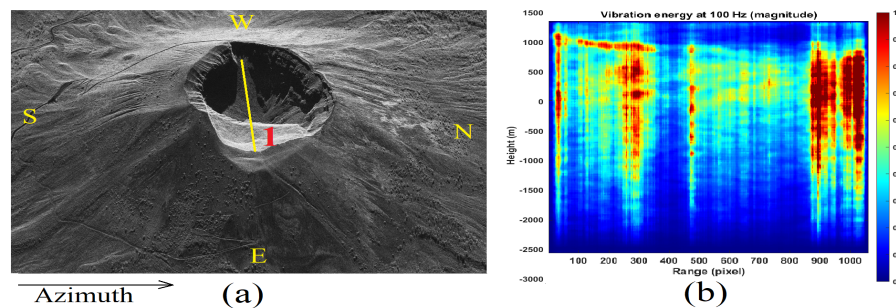


**Figure 6.** Range-line echographic tomography detailed result (magnitude). (a) SLC SAR image (in magnitude). (b) Tomographic result (in magnitude).

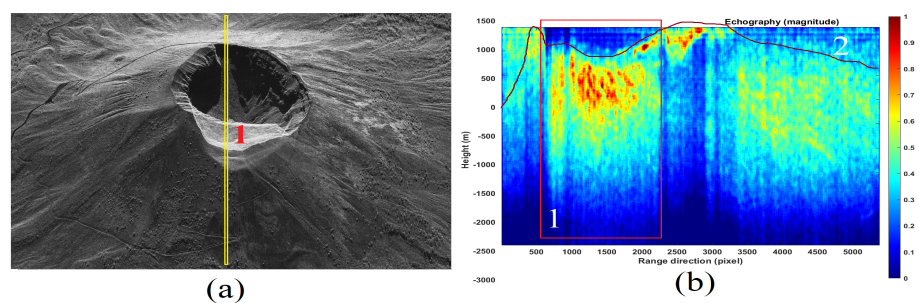
Figure 7a shows the SAR image (in magnitude) of Vesuvius according to a new tomographic line inserted, slightly more inclined, to cover as much as possible, in radar visibility, the volcano crater diameter, on the condition of having the greater scattering energy. On those pixels, we calculated the seismic tomogram visible in Figure 7b. In this case, the possible presence of a cap constituted by dense rocky material and the presence of an energetic gap where the seismic waves oscillate with less intensity is visible.

Figure 8a represents the SAR SLC image where the tomographic line 1 is shown where we investigate the acoustic response in depth. The result obtained, thus the tomography of the entire line is proposed in Figure 8b. The topographic height is correctly detected through line 2.

In Figure 9a, the detailed seismic tomography of the Vesuvius crater is depicted (particular of box numer 1 of Figure 8b), and details of the SAR image are proposed in Figure 9b. Figure 9c is the sonic tomogram of a range line spanning the entire crater. Through yellow arrows 3 and 4, pointing to the SAR image, two conduits are shown; finally, through arrow 4, the presence of a massive debris accumulation is detected. This facility appears to be composed of several layers having different physical compositions. The debris layers are detailed within circle 1 (visible in Figure 9b). The maximum depth of the layers is measured to be about 2 km deep, relative to the top surface of the volcano. Figure 10 is an overview of Vesuvius for which the seismic tomogram has been calculated through a purely azimuth-oriented line, which is visible in Figure 10a, and tracked through yellow line 1. The tomographic result is shown in Figure 10b, for which the main section is shown within the red circle visible in Figure 10a. The result shows probable magmatic fluid conduits, detected in terms of vibrational energy discontinuities. Figure 11 represents the tomographic result obtained considering an oblique section, visible in Figure 11a. For this case, the tomographic line is traced through yellow line 1. The proposed tomographic map shows the entire volcano internal section (Figure 11b). The tomogram was calculated at a higher resolution and taking into account a longer orbital variation.



**Figure 7.** Range-line echographic tomography result (magnitude). (a) SLC SAR image (in magnitude). (b) Tomographic result (in magnitude).



**Figure 8.** Range-line echographic tomography result (magnitude). (a) SLC SAR image (in magnitude). (b) Tomographic result (in magnitude). The yellow tomographic line is indicated by the number 1.

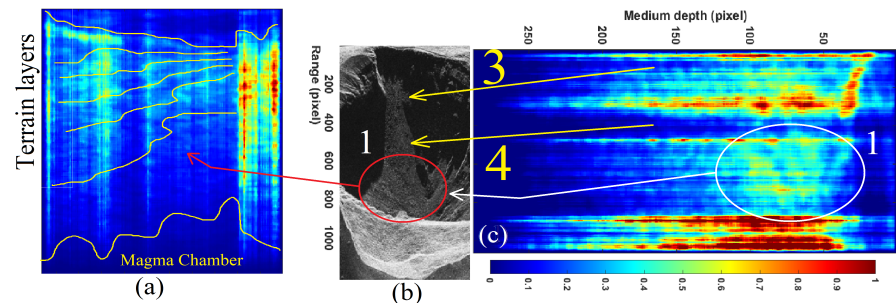


**Figure 9.** Range-line echographic tomography result (magnitude). (a) Tomographic result (in magnitude). (b) SLC SAR image (in magnitude). (c) Tomographic result (in magnitude).

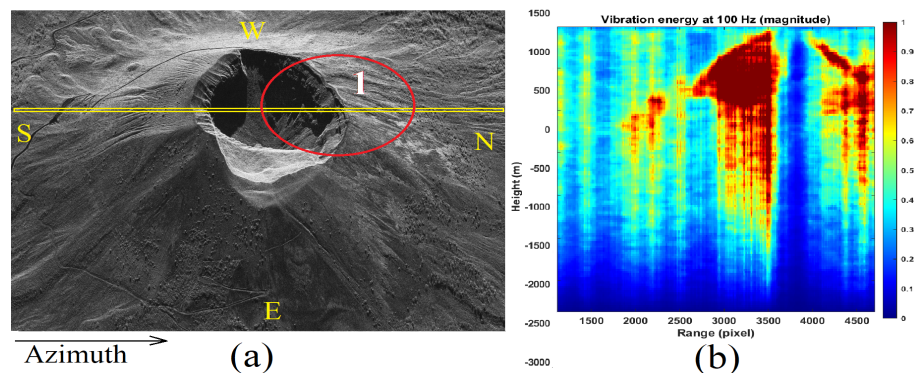


**Figure 10.** Range-line echographic tomography result (magnitude). (a) SLC SAR image (in magnitude). (b) Tomographic result (in magnitude). The yellow tomographic line is indicated by the number 1.

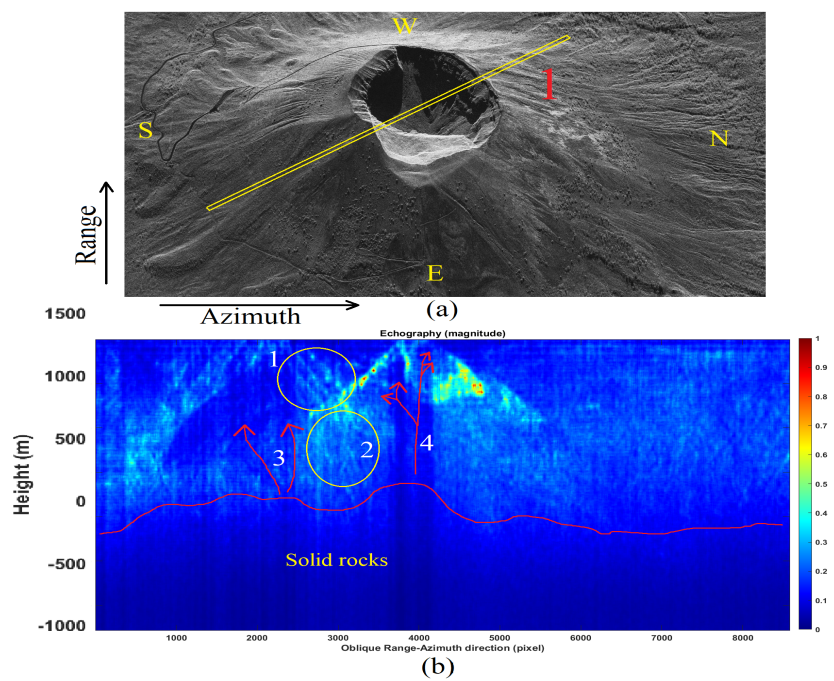


**Figure 11.** Range-azimuth line echographic tomography result (magnitude). (a) SLC SAR image (in magnitude). (b) Tomographic result (in magnitude). The yellow tomographic line is indicated by the number 1.

The following information is obtained from the calculated tomograms:

- The inner western volcano crater tomographic slopes consist of layered material, visible within yellow circle 1 of Figure 9b;
- The main volcano crater can be plugged by a cap of material consistent with vibration energy singularity, depicted within the yellow circle 2 of Figure 11b;
- The main conduits from the magma chamber rise from the east and west tomographic sections, indicated by arrows 3 and 4 of Figure 11b;
- The same results are obtained by calculating the sonic tomogram at a lower vibrational frequency, for which the result is visible in Figure 12.

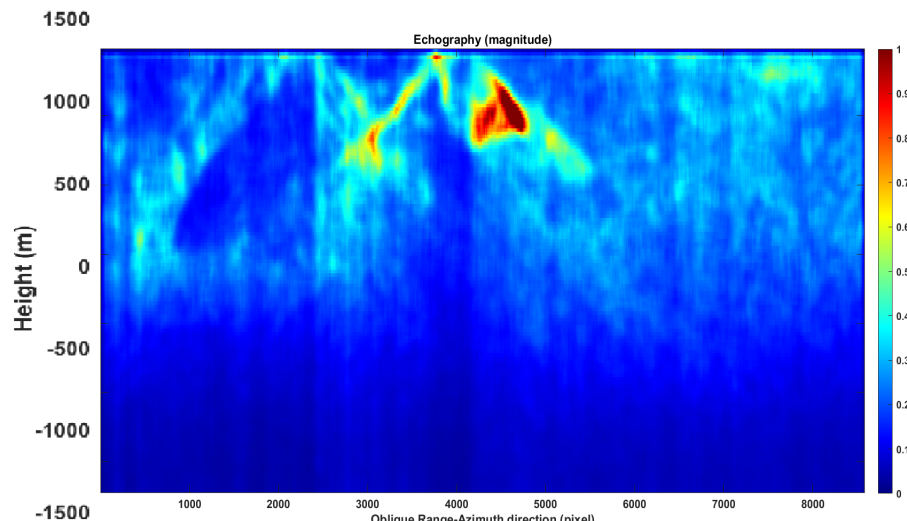


**Figure 12.** Range-azimuth line echographic tomography result (magnitude).

A detailed list of feeder conduits is proposed in Figure 13. These natural passages are made of material that does not resonate. We consider this characteristic as possible

magmatic fluid paths that a hypothetical new eruption might prefer. From the western side of the great crater, it is possible to edit 11 fractures. The ones belonging from 1 through 5 are located within the main crater, while fractures 9–11 may extend outside the crater. The complete list of possible magmatic fluid paths can be seen in Figure 13a. A detailed tomographic section of the fractures finishing inside the crater can be seen in Figure 13b, while a detailed tomogram of the upper magmatic fluid ducts is visible in Figure 13c–e, and finally some external magmatic fluid paths are depicted in Figure 13f.

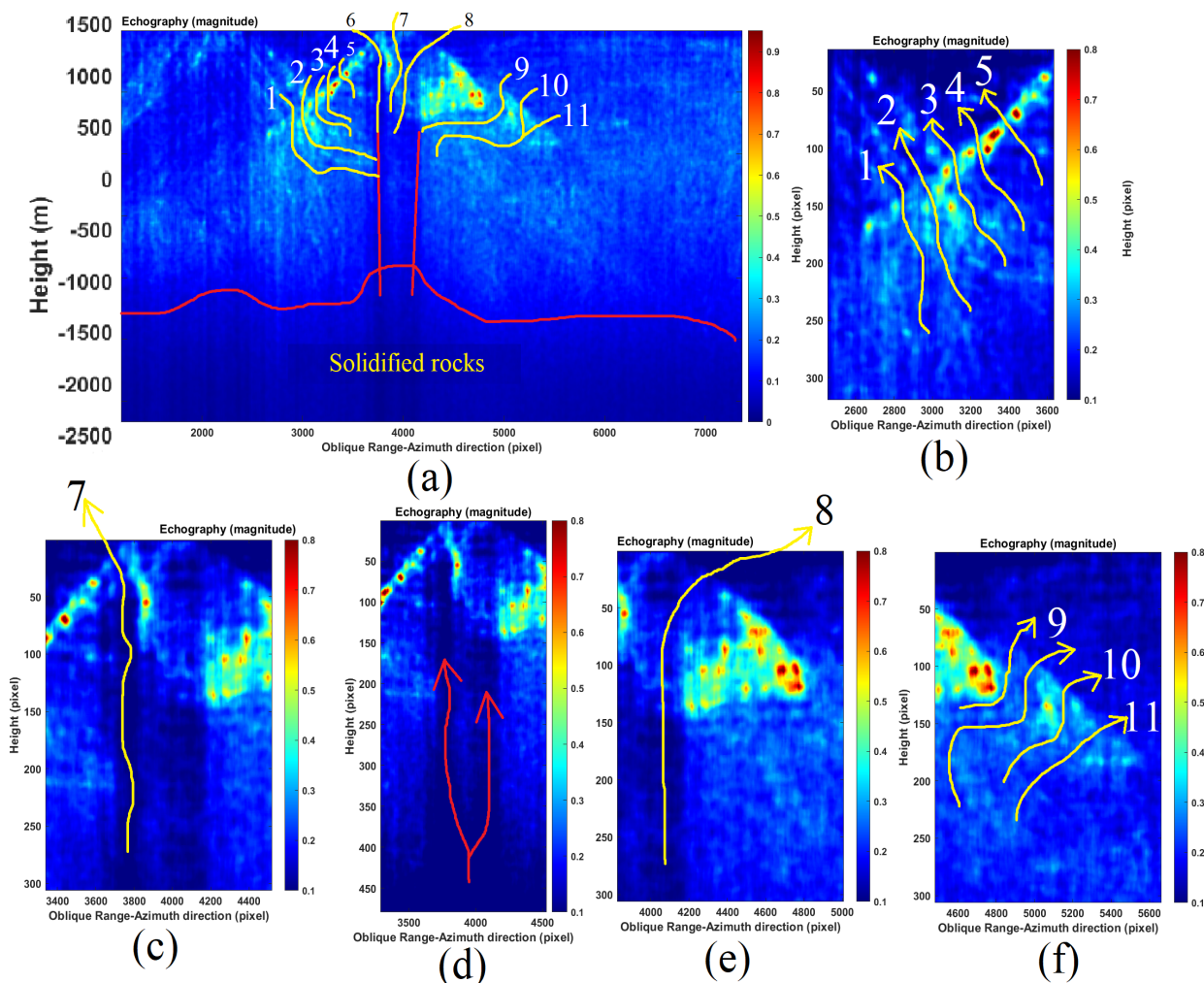


**Figure 13.** Tomographic results and analysis. (a) Tomographic analysis of the external eastern slope of Vesuvius, where potentially 11 magmatic fluid fractures are visible. At the bottom of the tomogram, the presence of a magma chamber is evident. (b) Tomographic results and analysis. (a) Tomographic analysis of the internal eastern slope of Vesuvius, where potentially five magmatic fluid fractures are visible. At the bottom of the tomogram, the presence of a magma chamber is evident. (c) Detail of the eastern slope showing an internal feeder conduit. (d) Detail of the deepest part of the conduit showing a splitting of the magmatic fluid conduit. (e) Detail of the external magmatic fluid conduit (upper part). (f) Detail of the eastern slope on the external side (lower part).

#### 4. Validation of the Sonic Tomographic SAR Results

##### 4.1. Topographic Validation

In this section, the topographic validation of the estimated tomograms is performed. The topographic elevation lines are provided by the digital elevation model (DEM) generated by the Shuttle Radar Topography Mission (SRTM). The topographic lines are superimposed on the estimated tomographic sections. In this specific case, the topographic line 1 visible in Figure 14a has been extrapolated from the global SRTM topographic surface,